Ultramicroscopy 168 (2016) 34–45

Contents lists available at ScienceDirect

Ultramicroscopy

journal homepage: www.elsevier.com/locate/ultramic

Geometrically necessary dislocation densities in olivine obtained using high-angular resolution electron backscatter diffraction

David Wallis [a,*], Lars N. Hansen [a], T. Ben Britton [b], Angus J. Wilkinson [c]

[a] Department of Earth Sciences, University of Oxford, South Parks Road, Oxford, Oxfordshire, OX1 3AN, UK
[b] Department of Materials, Imperial College London, Royal School of Mines, Exhibition Road, London SW7 2AZ, UK
[c] Department of Materials, University of Oxford, Parks Road, Oxford, Oxfordshire, OX1 3PH, UK

ARTICLE INFO

Article history:
Received 2 January 2016
Received in revised form
25 May 2016
Accepted 6 June 2016
Available online 8 June 2016

Keywords:
Electron backscatter diffraction
Cross-correlation
Olivine slip systems
Dislocation density
Geological materials
HR-EBSD

ABSTRACT

Dislocations in geological minerals are fundamental to the creep processes that control large-scale geodynamic phenomena. However, techniques to quantify their densities, distributions, and types over critical subgrain to polycrystal length scales are limited. The recent advent of high-angular resolution electron backscatter diffraction (HR-EBSD), based on diffraction pattern cross-correlation, offers a powerful new approach that has been utilised to analyse dislocation densities in the materials sciences. In particular, HR-EBSD yields significantly better angular resolution ($<0.01°$) than conventional EBSD ($\sim 0.5°$), allowing very low dislocation densities to be analysed. We develop the application of HR-EBSD to olivine, the dominant mineral in Earth's upper mantle by testing (1) different inversion methods for estimating geometrically necessary dislocation (GND) densities, (2) the sensitivity of the method under a range of data acquisition settings, and (3) the ability of the technique to resolve a variety of olivine dislocation structures. The relatively low crystal symmetry (orthorhombic) and few slip systems in olivine result in well constrained GND density estimates. The GND density noise floor is inversely proportional to map step size, such that datasets can be optimised for analysing either short wavelength, high density structures (e.g. subgrain boundaries) or long wavelength, low amplitude orientation gradients. Comparison to conventional images of decorated dislocations demonstrates that HR-EBSD can characterise the dislocation distribution and reveal additional structure not captured by the decoration technique. HR-EBSD therefore provides a highly effective method for analysing dislocations in olivine and determining their role in accommodating macroscopic deformation.

1. Introduction

The rheological properties of crystalline materials undergoing high-temperature creep are intimately linked to their dislocation contents and structures. As such, dislocation analysis is of significant interest for both materials and Earth sciences. Dislocations may be analysed by direct observation at the lattice-scale (e.g. by transmission electron microscopy, TEM [1]) or by decoration techniques at the grain- or aggregate-scales (e.g. by optical or scanning electron microscopy [2–4]). However, ongoing developments in analysis of electron backscatter diffraction (EBSD) data, collected in the scanning electron microscope (SEM), are providing new methods for quantitative analysis of dislocation densities and distributions over scales ranging from tens of nanometres up to millimetres [5–9]. EBSD-based dislocation density analysis is expanding in the materials sciences [10–12] with the advent of high-angular resolution EBSD (HR-EBSD), based on diffraction pattern cross-correlation, providing unprecedented sensitivity in measurements of lattice curvature and resulting estimates of dislocation density [9,13,14]. However, the application of quantitative EBSD-based dislocation density analysis to geological materials has been limited to date [8,15,16], and recently developed HR-EBSD methods have not yet, to the authors knowledge, been applied to common rock-forming minerals. In this contribution, we develop and test the ability of HR-EBSD to derive dislocation density estimates for olivine, the most abundant mineral in Earth's upper mantle.

Olivine constitutes typically $>60\%$ of Earth's upper mantle, and therefore olivine rheology exerts a first order control on large-scale geodynamic processes such as mantle convection [17–19], formation of mantle shear zones [20,21] and subduction of oceanic lithosphere [22]. Olivine deformation in laboratory experiments, at strain rates typically $>10^{-7}\,s^{-1}$, has been interpreted to occur by a range of deformation mechanisms, including dislocation creep [23–26] and dislocation- or diffusion-accommodated grain boundary sliding [27–32], with the rate-controlling mechanism

* Corresponding author.
E-mail address: davidwa@earth.ox.ac.uk (D. Wallis).

http://dx.doi.org/10.1016/j.ultramic.2016.06.002

varying with material properties (e.g. grain size and composition) and thermomechanical conditions (e.g. temperature, stress state, and strain rate). To describe natural deformation at typical strain rates of 10^{-10}–10^{-15} s^{-1}, laboratory-derived flow laws must be greatly extrapolated. Confidence in such extrapolations can only be gained if the same fundamental deformation mechanisms and processes can be demonstrated to have occurred in both the experimental and natural materials. These considerations motivate detailed dislocation analysis (dislocation types, densities, and distributions) in order to model and interpret their role in accommodating strain.

Several methods for analysing dislocations in olivine have been developed, providing useful tools for investigating the mechanisms and conditions of deformation. Early work on olivine dislocations relied primarily on examination of slip traces or etch pits in deformed crystals in order to identify slip system types and the conditions under which dislocation glide occurs [33–35]. Subsequent TEM studies allowed olivine dislocations to be investigated in greater detail, permitting initial interpretations of dislocation dynamics [36–39]. The development of a technique for decorating dislocations by oxidation [2] allowed larger-scale dislocation structures and densities to be readily observed [40,41], and dislocations naturally decorated through similar processes were identified [42]. Decoration of dislocations in experimentally deformed single crystals of olivine allowed the important observations that increasing differential stress increases the dislocation density, decreases the minimum glide loop radius, and decreases the tilt-boundary spacing, providing piezometric relationships for investigating stress conditions of naturally deformed, olivine-rich rocks [40,41]. An inverse relationship between dislocation density and subgrain size has also been established based on observations of decorated dislocations in naturally deformed olivine [43].

Although decoration by oxidation provides a simple method to investigate dislocation densities and distributions in olivine, dislocation types can typically only be inferred and no information on associated lattice rotations, elastic strain or residual stress can be derived. Recent studies have employed more sophisticated techniques, such as TEM electron tomography [44] and geometric phase analysis [45] to discern dislocation types and quantify strain fields, but are typically limited to sample areas less than 1 μm^2. However, HR-EBSD provides both the high angular resolution necessary to resolve dislocation densities, distributions, residual stresses and elastic strains, as well as the large areal coverage of EBSD maps, typically up to a few hundred μm^2 [9,13,46,47].

HR-EBSD-based dislocation analysis has been successfully applied to a range of materials, including copper [48], titanium [49], Ti–6Al–4V [50] and yttria-stabilised zirconia [51]. Unfortunately, due to the abundant slip systems available in these previously investigated materials, the calculation of densities of different types of dislocations is non-unique as many combinations are available that can generate the measured lattice orientation gradients (e.g. for bcc iron, densities of 16 dislocation types can be combined to fulfil only six measurable curvature components), and therefore additional constraints must be imposed [9]. In contrast, olivine exhibits very few dislocation types due to its relatively low crystal symmetry (orthorhombic) and long [010] direction (a=4.8 Å, b=10.2 Å, c=6.0 Å), effectively precluding slip systems with [010] Burgers vectors [52,53]. As a result, slip system determinations in olivine are better constrained than in applications to higher symmetry minerals.

The aim of the present study is to develop the application of HR-EBSD to dislocation analysis in olivine by testing the sensitivity limits of the technique under a range of data acquisition settings and dislocation-density inversion techniques. We compare HR-EBSD-derived dislocation densities to those from Hough-based analysis and also to images of decorated dislocations to further demonstrate the capabilities of the technique. The results open opportunities for future work on olivine dislocation densities, substructure and evolution, with the advantages of large spatial coverage, high angular resolution, and relatively simple sample preparation that HR-EBSD provides.

2. Methods

2.1. Relating lattice curvature to geometrically necessary dislocation density

EBSD-based dislocation analysis exploits large volumes of lattice orientation data to characterise intracrystalline curvature resulting from the presence of dislocations. The portion of the dislocation density that contributes to lattice curvature at the scale of observation is classified as the geometrically necessary dislocation (GND) density. A Burgers circuit construction around an arbitrary group of dislocations reveals that only a fraction of them contribute to the net Burgers vector and thus correspond to the GND density. While, in contrast, other dislocation structures such as dipoles, multipoles, and loops result in no lattice curvature and a null net Burgers vector at scales larger than the Burgers circuit under consideration. This latter contribution to the dislocation density is classified as the statistically stored dislocation (SSDs) density [54,55]. Although individual defects cannot be unambiguously assigned as GNDs or SSDs, the contributions to the total dislocation density are unambiguous.

The relationship between gradients in lattice orientation (g) and components of Nye's dislocation density tensor (α_{ij}) is given by

$$\alpha_{ij} = e_{ikl} g_{jl,k} \tag{1}$$

where e_{ikl} are components of the permutation tensor, and the comma denotes partial differentiation with respect to the subsequent index [6,55]. The elements of α_{ij} are related to the densities (ρ^s) of $s_{\max}$ different types of dislocation through

$$\alpha_{ij} = \sum_{s=1}^{s_{max}} \rho^s b_i^s l_j^s \tag{2}$$

where $\mathbf{b}^s$ is the Burgers vector and $\mathbf{l}^s$ is the unit line direction of the sth dislocation type [6,9]. This analysis assumes that long-range elastic strain gradients are negligible compared to the lattice rotation gradients [54]. This assumption is indeed the case for the samples analysed here, for which the elastic strain gradients are on the order of 1% of the lattice rotation gradients.

2.2. Resolving low densities of geometrically necessary dislocations using high angular resolution EBSD

Lattice orientation gradients are readily determined from EBSD data based on angular misorientations between adjacent measurements. The precision of such misorientations provides a first-order control on the precision of resulting GND density estimates. During conventional EBSD analysis, angular uncertainties in individual orientation measurements are typically $\sim$0.5° and arise from the determination of band positions in the diffraction pattern using a Hough transform. For a measurement spacing (i.e., EBSD step size) of 200 nm, this precision results in a minimum measureable GND density of $\sim 10^{14}$ m^{-2} [13,47]. Sensitivities of this magnitude are sufficient for resolving high GND densities typical of experimentally deformed metals [5,6] and can resolve high GND density subgrain structures in geological minerals [8]. Nonetheless, geological materials deformed at low stress and high

temperature typically contain dislocation densities of $\sim 10^{-10}$–10^{-12} m^{-2} [40,41], which cannot be resolved using conventional EBSD analysis.

The recently developed HR-EBSD approach uses an alternative method to determine misorientations by directly comparing diffraction patterns from neighbouring points in an EBSD map [13,14]. This method cross-correlates regions of interest in the diffraction patterns with the same regions in a specified reference pattern, yielding the rotations and elastic strains responsible for the difference in the patterns. HR-EBSD can be sensitive to rotations of less than 0.01°, resulting in improved precision in subsequent dislocation density estimates and the ability to resolve very low-misorientation microstructures [9,13,47]. Jiang et al. [47] established that the noise floor (i.e., the minimum measureable value) for measurement of GND density varies with EBSD acquisition settings, such as pattern binning and step size, that are commonly adjusted to optimise the speed and accuracy of mapping. They demonstrated that binning of pixels in electron backscatter diffraction patterns (EBSPs) from undeformed silicon, and the associated decrease in angular resolution, results in a relatively modest increase in the GND density noise floor. In contrast, decreasing the mapping step size increases the noise floor much more significantly due primarily to increasing uncertainty in orientation gradients and also due to increasing the apparent ratio of GND to SSD density within the Burgers circuit. Thus, increasing the step size potentially offers an opportunity to resolve lower average GND densities, although a lower noise floor comes at the expense of spatial resolution.

2.3. Experimental procedure

2.3.1. Specimen preparation

To demonstrate the application of HR-EBSD to olivine, we utilise two specimens deformed in a Paterson gas-medium apparatus at the University of Minnesota. The first is a single crystal of San Carlos olivine ($\sim Fo_{90}$), PI-1433. This specimen was deformed in triaxial compression at 1000°C and 388 MPa differential stress to 8% finite strain. The primary compressive stress was oriented to roughly bisect [010] and [001]. The second is a polycrystalline specimen of Fo_{50}, PT-0652, which was deformed initially in torsion at 1200°C and 112 MPa to 10.6 shear strain, followed by extension at stresses between 78 MPa and 155 MPa to a total extensional strain of ~10% [56]. The sample was then sectioned on a plane tangential to the cylindrical sample surface. Both specimens were polished using diamond suspensions down to 0.25 μm grit size and finished with ~15–30 min polishing on 0.03 μm colloidal silica. Dislocations in PT-0652 were decorated by the oxidation technique of [2], and then the surface was briefly re-polished to remove the thin oxidised surface rind, leaving the dislocations and boundaries that oxidised to greater depths. The decorated dislocations were imaged using forescattered electron detectors before an EBSD map of the same area was collected. Precipitation of oxides in the decoration process may induce elastic strains due to the change in volume, but the precipitates are not envisioned to induce significant lattice rotations, and therefore should not affect the calculation of GND densities.

To investigate the ultimate sensitivity of the GND density calculations, we also examined an undeformed single crystal of silicon and an undeformed single crystal of San Carlos olivine (MN1). The latter was decorated and prepared as above, and the decorated dislocations were imaged using backscattered electrons. With the exception of rare subgrain boundaries, dislocation densities were observed to be $< 10^{10}$ m^{-2}. No subgrain boundaries were present in the area subsequently mapped.

2.3.2. Data acquisition

EBSD data were acquired using Oxford Instruments AZtec software on an FEI Quanta 650 field-emission gun SEM equipped with an Oxford Instruments Nordlys S EBSD camera in the Department of Earth Sciences at the University of Oxford. Operating conditions were 70° specimen tilt, 8.4–11.9 mm working distance and 20–30 kV accelerating voltage. Electron backscatter patterns (EBSPs) were processed to remove the background signal by division and saved as 8 bit TIFF files for subsequent HR-EBSD analysis.

2.3.3. Methods of determining GND content

Due to the general insensitivity of EBSD measurements to lattice orientation gradients in the direction normal to the specimen surface, only five elements of α_{ij} can be determined directly (α_{12}, α_{13}, α_{21}, α_{23}, and α_{33}), along with the difference between two of the remaining unknown elements, i.e., $\alpha_{11}-\alpha_{22}$ [7]. As such, Eq. (2) can be written in the form

$$\mathbf{A}\boldsymbol{\rho} = \boldsymbol{\lambda} \tag{3}$$

where $\boldsymbol{\rho}$ is a vector of densities for all s_{max} dislocation types, and $\boldsymbol{\lambda}$ is a vector of measureable lattice curvature components. $\mathbf{A}$ is a $6 \times s_{max}$ matrix in which each column contains the dyadic of the Burgers vector and unit line direction of the sth dislocation type. Assuming that the lattice rotation gradients are significantly larger than the elastic strain gradients [9], Eq. (3) can be expanded to link directly between $\boldsymbol{\rho}$ and the six measurable curvature components, $\frac{\partial w_{jk}}{\partial x_i}$ [49], as

$$\begin{bmatrix} b_1^1 l_1^1 - 1/2 b^1 l^1 & \cdots & b_1^s l_1^s - 1/2 b^s l^s \\ b_1^1 l_2^1 & \cdots & b_1^s l_2^s \\ b_1^1 l_3^1 & \cdots & b_1^s l_3^s \\ b_2^1 l_1^1 & \cdots & b_2^s l_1^s \\ b_2^1 l_2^1 - 1/2 b^1 l^1 & \cdots & b_2^s l_2^s - 1/2 b^s l^s \\ b_2^1 l_3^1 & \cdots & b_2^s l_3^s \end{bmatrix} \begin{bmatrix} \rho_1 \\ \vdots \\ \rho_s \end{bmatrix} = \begin{bmatrix} \frac{\partial w_{23}}{\partial x_1} \\ \frac{\partial w_{31}}{\partial x_1} \\ \frac{\partial w_{12}}{\partial x_1} \\ \frac{\partial w_{23}}{\partial x_2} \\ \frac{\partial w_{31}}{\partial x_2} \\ \frac{\partial w_{12}}{\partial x_2} \end{bmatrix}. \tag{4}$$

Although these six available terms provide useful information about the GND content [5–8], information about the densities of different dislocation types is incomplete. As an alternative, the density of different dislocation types can be solved for in a least-squares sense (i.e., using the L2-norm and referred to from here on simply as L2) following [57]

$$\boldsymbol{\rho} = \mathbf{A}^{\mathrm{T}}\left(\mathbf{A}\mathbf{A}^{\mathrm{T}}\right)^{-1}\boldsymbol{\lambda}. \tag{5}$$

This approach yields the average dislocation density for the sth dislocation type in which dislocations with opposite sign (i.e., generating opposite curvatures) are considered simultaneously. For a mineral with six dislocation types, this approach defines $\mathbf{A}$ as a 6×6 matrix. Alternatively, dislocations with opposite sign can explicitly be separated into two densities, one with only positive values and the other with only negative values. Thus, for a mineral with six dislocation types, $\mathbf{A}$ is defined as a 6×12 matrix. This case is valuable for inversion methods with constraints on the sign of the values in $\boldsymbol{\rho}$.

For high-symmetry materials with >6 available dislocation types, the L2 approach defined in Eq. (5) does not have a unique solution based on minimising the least squares misfit in dislocation density alone. In such instances, minimisation of a different objective function, such as dislocation line energy or length can be

Table 1
Olivine slip systems used in dislocation density calculations.

Dislocation type	Slip system
Edge	(010)[100]
Edge	(001)[100]
Edge	(100)[001]
Edge	(010)[001]
Screw	[100]
Screw	[001]

employed. For instance, Wilkinson and Randman [9] investigated the highly under-constrained system of a two-dimensional EBSD map of bcc iron, in which case, the dislocation densities of different dislocation types must be estimated from 32 unknowns (positive and negative curvatures arising from 16 dislocation types). To discriminate between different combinations of dislocation densities that all reproduce the observed lattice curvatures, they employed an optimisation scheme (referred to from here on as L1) that follows Eq. (5) while simultaneously minimising the total line energy of the dislocations.

Olivine has the advantage of a relatively small number of slip systems, leading to better constrained GND density inversions. For olivine, we only consider dislocations associated with the four primary slip systems observed in samples deformed in high-temperature creep tests (Table 1), including both edge and screw dislocations (for a review of observed dislocation types see [53]), which results in six types of dislocations in total (or 12 if positive and negative dislocation types are considered separately).

To determine the optimal inversion method for olivine, we performed systematic tests of several inversion methods. We implemented high-level functions available in MATLAB®, including the '*linprog*' function for the L1 scheme and '*pinv*' (pseudoinversion) and '*lsqnonneg*' (least squares non-negative) functions for the L2 scheme. Following Wilkinson and Randman [9], the L1 scheme includes weights in the optimisation to minimise the (isotropic) line energy for edge and screw dislocations (E_{edge} and E_{screw} respectively) according to

$$E_{\text{edge}} \propto \boldsymbol{b}^2 \tag{6}$$

and

$$E_{\text{screw}} \propto \frac{\boldsymbol{b}^2}{1-\nu} \tag{7}$$

where ν is the Poisson's ratio.

The L1 scheme requires the curvature to be exactly described by the resulting dislocation densities, which may not always be possible with the limited number of slip systems in olivine. Thus, we used the six dislocation types in Table 1 along with three 'fictitious' dislocation types with Burgers vectors parallel to [010] to yield nine total dislocation types. These fictitious dislocation types were assigned Burgers vectors with lengths multiple orders of magnitude larger than the other dislocation types. As a result, negligible densities of these dislocation types are invoked to accommodate the input curvatures. The L1 scheme also requires the signs of all of the dislocation densities in $\boldsymbol{\rho}$ to be positive, and therefore positive and negative dislocation are considered separately (i.e., $\mathbf{A}$ is expanded to be a 6×18 matrix).

We also included the three fictitious dislocation types in some tests of the *pinv* and *lsqnonneg* functions, although their inclusion is not required. These results are referred to as pinv18, and lsq18 respectively, for which the label 18 denotes the number of columns in **A.** For *pinv*, it is also not necessary to separate positive and negative dislocations. Therefore, we additionally grouped dislocations of different sign together for several tests, yielding a matrix **A** with 6 columns if no fictitious slip systems are used (pinv6) or 9 columns if the fictitious slip systems are used (pinv9). The inversion methods used are summarised in Table 2.

Table 2
Summary of inversion methods for estimating dislocation densities.

Inversion method	Function	Number of slip systems	Size of A in Eqs. (3) and (5)
L1	linprog	9	6×18
pinv6	pinv	6	6×6
pinv9	pinv	9	6×9
pinv12	pinv	6	6×12
pinv18	pinv	9	6×18
lsq12	lsqnonneg	6	6×12
lsq18	lsqnonneg	9	6×18

We also tested the effect of crystal orientation on the inversion results. To do so, we assumed a GND density of 10^{12} m^{-2} was present on a particular slip system and forward calculated the expected lattice curvature. We then determined the values of $\boldsymbol{\lambda}$ (Eqs. (3) and (5)) that would be measured by EBSD mapping a surface at a specified orientation relative to the crystallographic axes. Finally, we used the inversion methods described above to attempt to recover the input GND densities from the $\boldsymbol{\lambda}$ values that would be accessible from EBSD measurements. By carrying out this procedure for multiple surface orientations, the effect of crystal orientation on the inversion results can be tested. In addition to carrying out the forward calculation with only one non-zero GND density, we also carried out this procedure assuming a GND density of 10^{12} m^{-2} was present for all of the six real olivine dislocation types.

2.3.4. Testing the effect of varying EBSD acquisition settings

To test the effect of varying EBSD acquisition settings on both calculated dislocation densities and spatial resolution of dislocation structures, we performed a systematic analysis of EBSD datasets from three specimens: an undeformed Si standard (50×50 points at 0.5 μm step size and 67×42 points at 8 μm step size), an undeformed olivine single crystal (MN1; 500×400 points at 1 μm step size and 30×21 points at 20 μm step size), and a deformed olivine single crystal (PI-1433; 247×214 points at 1 μm step size). All original datasets were collected without binning of EBSP pixels.

We sub-sampled the original EBSD datasets to investigate the effects of mapping the same areas with larger step sizes and greater EBSP binning. To simulate larger step sizes, we under-sampled the data, using only a regularly spaced fraction of data points from the original datasets. To simulate a range of pattern binning (2×2, 4×4, and 8×8 pixels), we reduced the resolution of the original stored EBSPs by averaging groups of adjacent pixels. Investigations of the effect of pattern binning were only carried out on datasets with 8–10 μm step sizes. Repeatedly sub-sampling the same dataset has advantages over collecting multiple datasets as it is more efficient and allows exactly the same measurement points to be analysed in each case. For this series of tests, maps of dislocation density were produced using the pinv6 inversion method for olivine and L1 scheme for silicon.

To examine the effect of increasing step size on the ability to resolve different dislocation structures, we performed a similar under-sampling analysis on a map collected over an area in which dislocations had been decorated by oxidation and were therefore detectible in forescattered electron images. For this series of tests, maps of dislocation density were also produced using the pinv6 inversion method. The original dataset with 0.25 μm step size was under-sampled and reanalysed to generate additional datasets with 1 and 2 μm step sizes.

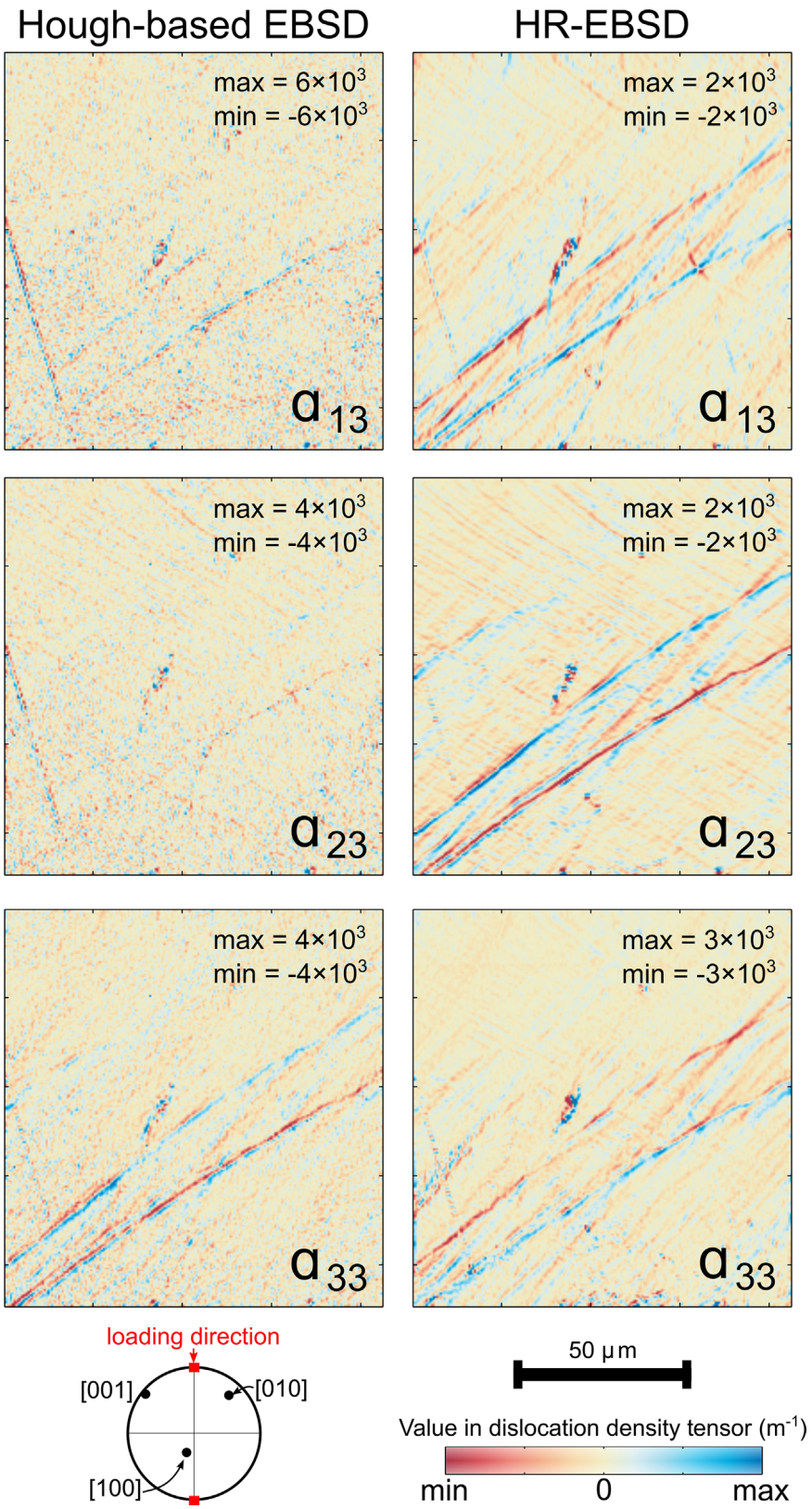

Fig. 1. Maps of α_{i3} components of the dislocation density tensor obtained by either Hough-based EBSD or HR-EBSD for olivine single crystal PI-1433. Lower hemisphere equal area projection presents the crystal orientation and compressional loading direction in the map reference frame. The maps consist of 212 × 223 points collected at 1.25 μm step size and 2 × 2 EBSP pixel binning. (For interpretation of the references to color in this figure, the reader is referred to the web version of this article.)

3. Results

3.1. Comparison between conventional EBSD and HR-EBSD

A comparison between the α_{i3} components of the dislocation density tensor obtained by Hough-based EBSD and HR-EBSD is presented in Fig. 1. The HR-EBSD results exhibit distinct and well-resolved GND substructure, including prominent boundaries (oriented top-right to bottom-left) and less pronounced, more closely spaced bands (oriented top-left to bottom-right), both of which

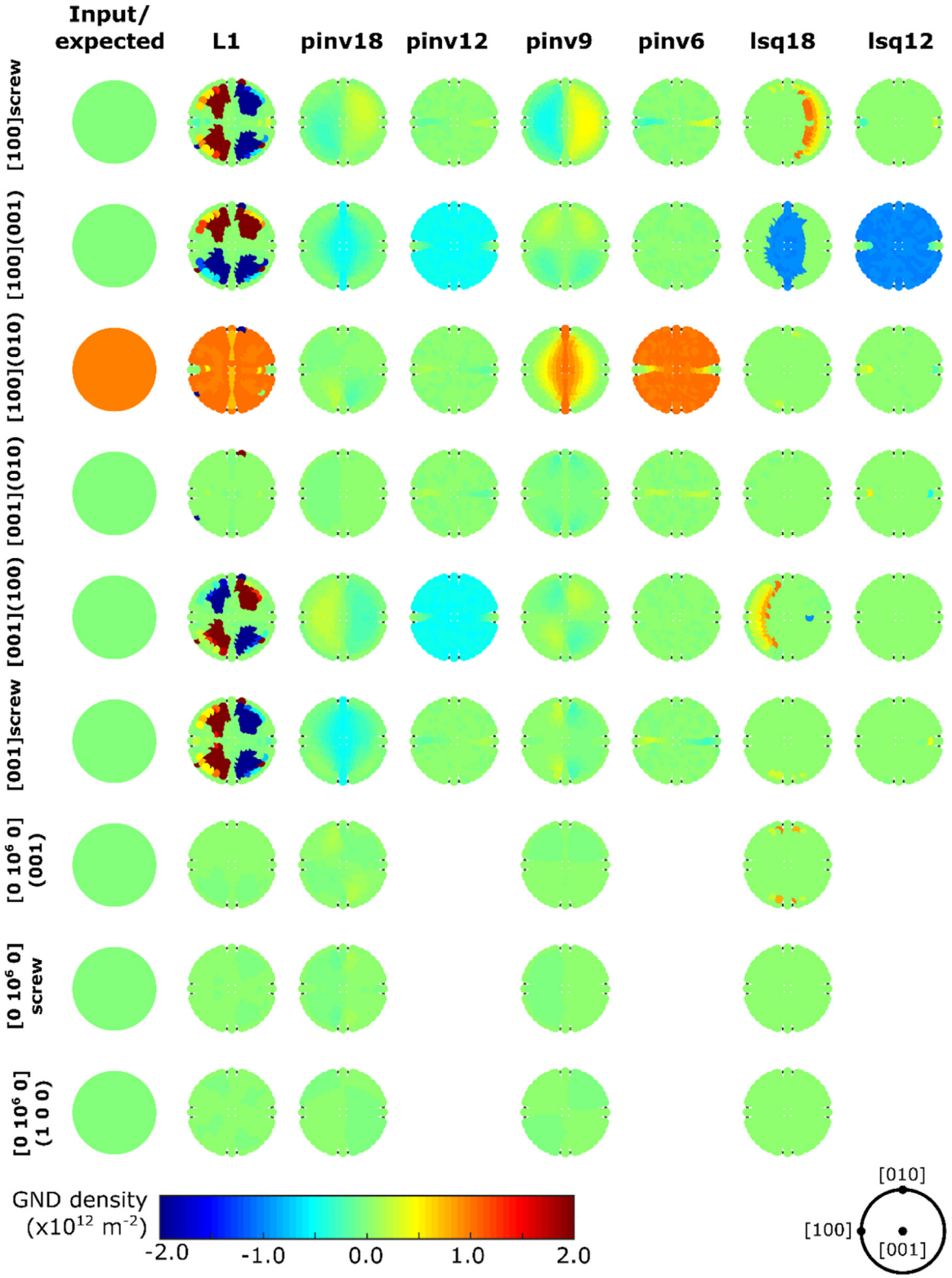

Fig. 2. Olivine GND densities recovered by each inversion method using an input curvature corresponding to 10^{12} m^{-2} on the (010)[100] slip system (i.e. third row). The location of each point represents the normal to the hypothetical specimen surface orientation in the crystal reference frame plotted in the lower hemisphere, and the colour represents the calculated GND density. The crystal reference frame is given in the lower right. In the case of ideal GND recovery, plots on the third row should be orange and all other plots green. (For interpretation of the references to color in this figure legend, the reader is referred to the web version of this article.)

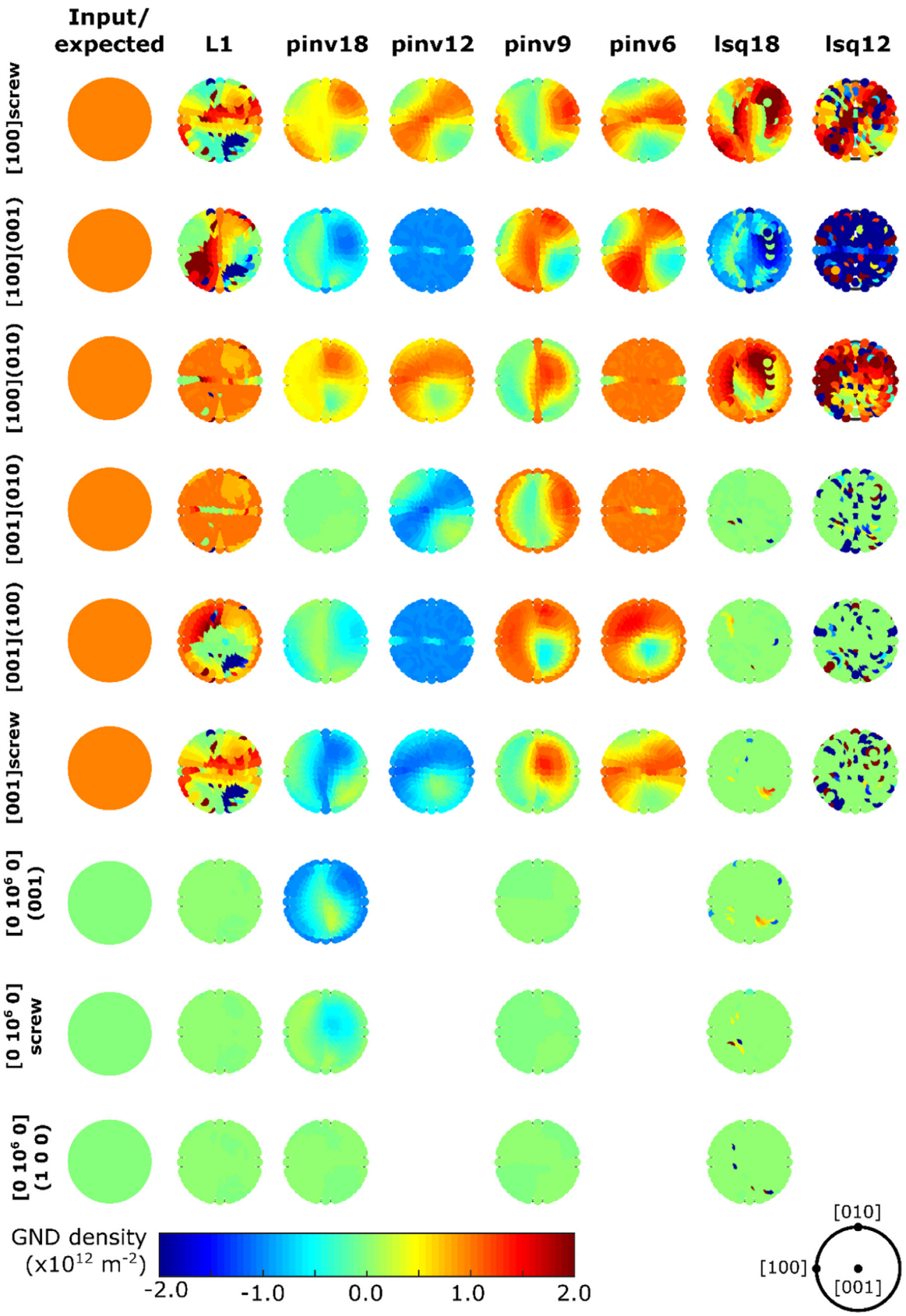

Fig. 3. Olivine GND densities recovered by each inversion method using an input curvature corresponding to 10^{12} m^{-2} on each real slip system (i.e. top six rows). The location of each point represents the normal to the hypothetical specimen surface orientation in the crystal reference frame plotted in the lower hemisphere, and the colour represents the calculated GND density. The crystal reference frame is given in the lower right. In the case of ideal GND recovery, plots on the top six rows should be orange and plots on the lower three rows green. (For interpretation of the references to color in this figure legend, the reader is referred to the web version of this article.)

are in orientations consistent with slip-systems predicted to be activated by the loading direction (compression direction top to bottom). In contrast, the Hough-based results lack many of the structures visible in HR-EBSD results. In particular, the α_{23} map lacks the prominent boundaries, and the finer bands are only subtly resolved. Similarly, the HR-EBSD maps largely lack visible background noise, whereas noise in the Hough-based maps obscures much of the detail. Note that these results are not affected by the differences in figure colour scaling.

3.2. Inversion methods and their orientation dependence

The extent to which each inversion method is able to recover the synthetic input GND density is illustrated in Figs. 2 and 3. Fig. 2 presents the GND densities recovered from curvatures corresponding to an input of 10^{12} m^{-2} GND density on the (010)[100] slip system (one of the most common in naturally deformed olivine). In the case of perfect inversion, each plot corresponding to this slip system (i.e. row three in Figs. 2 and 3) should be coloured orange, and all the other rows should be entirely green. The trial of pinv6 recovered GND densities very similar to the input for all specimen surface orientations except those parallel to [100]. Similarly, the L1 scheme successfully recovered most of the input GND densities, but also erroneously yielded significant densities in four other dislocation types. Other inversion methods recovered lower densities of GNDs than the input but distributed over multiple slip systems. The trial of lsq12 yielded dislocation densities of similar magnitude to the input but of the opposite sign and on a different slip system, (001)[100]. None of the inversion methods invoked significant quantities of the 'fictitious' slip systems. A similar set of results was obtained regardless of the dislocation type used as an input, as long as it was one of the six real dislocation types.

Fig. 3 presents the GND densities calculated from curvatures corresponding to an input of 10^{12} m^{-2} for all six of the real olivine dislocation types, simultaneously. In the case of accurate inversion for GND densities, each plot corresponding to the real dislocation types (i.e. the top six rows) should be coloured orange, and the bottom three rows should be entirely green. It should be noted that each calculated GND density in Fig. 3 results from (1) curvature associated with GND densities input for that dislocation type and (2) curvature erroneously generated by input GND densities of other dislocation types (as seen more clearly when inputting only one dislocation type, e.g. Fig. 2).

As in the case of an input GND density for only one dislocation type (Fig. 2), the results from pinv6 in Fig. 3 most closely match the input. The GND densities retrieved are in excellent agreement with the input for the majority of specimen orientations. The L1 results yield similar distributions to those from pinv6, but with significant noise resulting from the superposition of the erroneous GND densities (as apparent in Fig. 2). The other inversion methods clearly perform worse at recovering the input GND densities than L1 and pinv6.

It should be noted that the technique is insensitive to edge dislocations in a small range of orientation space in which the Burgers vector is normal to the specimen surface (i.e. green horizontal flashes in Fig. 2; also Fig. 4). In contrast, screw dislocations are related to two different orientation gradients, such that their full curvature is only measurable on planes normal to the Burgers vector (Fig. 4).

3.3. Varying EBSD acquisition settings and comparison to decorated dislocations

The effect of varying mapping step size and pattern binning on the calculated mean GND density is presented in Fig. 5. The mean GND densities for undeformed olivine and undeformed silicon are within error and are taken to represent the noise floor inherent in the technique. The mean GND densities of olivine deformed at 388 MPa differential stress are approximately an order of magnitude greater than those of the undeformed samples at equivalent step sizes. Calculated mean GND densities decrease systematically with increasing step size between 0.5 and 20 μm (Fig. 5a).

The GND density detected also varies with EBSP binning. As EBSP pixel binning is increased up to 8×8, the calculated mean GND densities in the undeformed samples increase slightly from $\sim 1 \times 10^{11}$ m^{-2} to $\sim 4 \times 10^{11}$ m^{-2} (Fig. 5b). This increase is presumably due to decreasing angular resolution resulting in increasing noise. In contrast, the mean GND density of the deformed olivine, which exhibits overall higher GND density than undeformed olivine, is relatively insensitive to the effects of increasing EBSP binning, with values remaining at $\sim 2 \times 10^{12}$ m^{-2} regardless of the degree of binning (Fig. 5b). Overall the impact of varying EBSP binning on the estimated GND density is minor compared to the impact of varying step size.

The effect of varying EBSD step size on the ability to resolve a range of dislocation structures is presented in Fig. 6. The forescattered electron image depicts decorated dislocations present both as discrete dislocations in a variety of orientations distributed throughout grain interiors and also arranged into straight or gently curved subgrain boundaries. High-angle grain boundaries are evident from the more prominent oxidation. The GND density map collected with 0.25 μm step size exhibits comparable structure to the forescattered electron image. Both subgrain boundaries and regions of high dislocation density visible in the electron image correspond to regions of high GND densities in the HR-EBSD map. However, there are areas of high GND density in the HR-EBSD map that lack corresponding dislocations in the electron image. This is

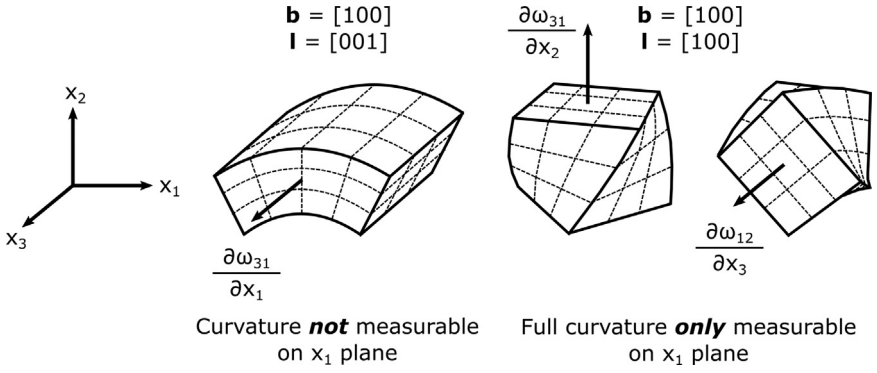

Fig. 4. Curvatures arising from edge and screw dislocations with [100] Burgers vectors. Curvature arising from edge dislocations is not measurable on planes normal to the Burgers vector. Screw dislocations are associated with two rotation components, so their full curvature can only be measured on planes normal to the Burgers vector.

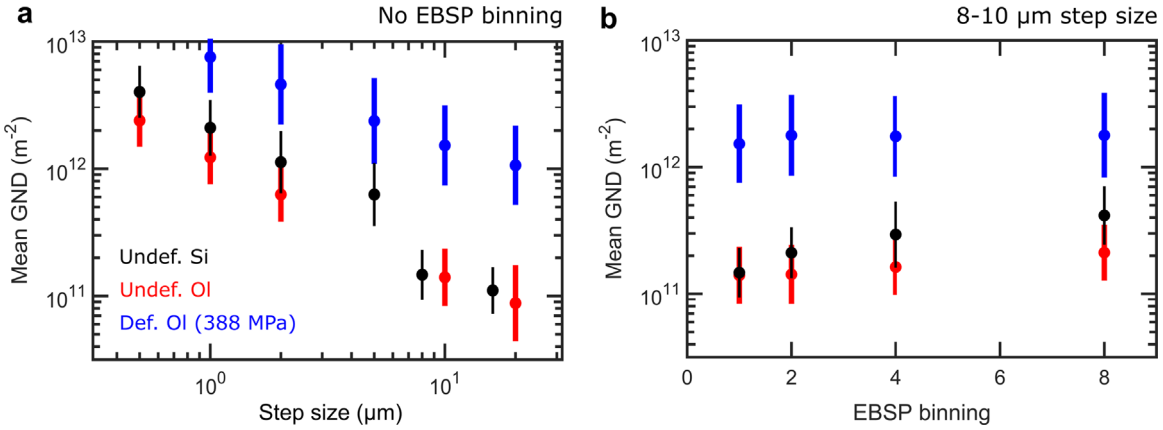

Fig. 5. Variation in estimated geometrically necessary dislocation (GND) density for single crystals of undeformed silicon (black), undeformed olivine (red) and deformed olivine (blue) as a function of (a) EBSD mapping step size and (b) EBSP pixel binning. EBSPs in (a) were collected with no binning and original map sizes were in the range 30×21 points to 500×400 points. Both were subsequently reduced by under-sampling. Maps in (b) have 8–10 μm step sizes and ranged from 25×20 to 67×42 points. Error bars indicate one standard deviation of the measurements within each map area. (For interpretation of the references to color in this figure legend, the reader is referred to the web version of this article.)

the case for both distributed dislocations (e.g. bottom centre) and subgrain boundaries (e.g. centre right). This apparent absence of oxidation is likely due to these dislocations lacking a rapid oxygen diffusion pathway to the specimen surface during oxidation (N.B., the imaged surface was internal to the specimen during oxidation prior to polishing, so dislocations intersecting the observation surface may not have intersected the oxidised surface). HR-EBSD-derived GND density maps therefore have potential to reveal more dislocation structure than can be imaged by the traditional oxidation decoration method. Note that the noise floor at this step

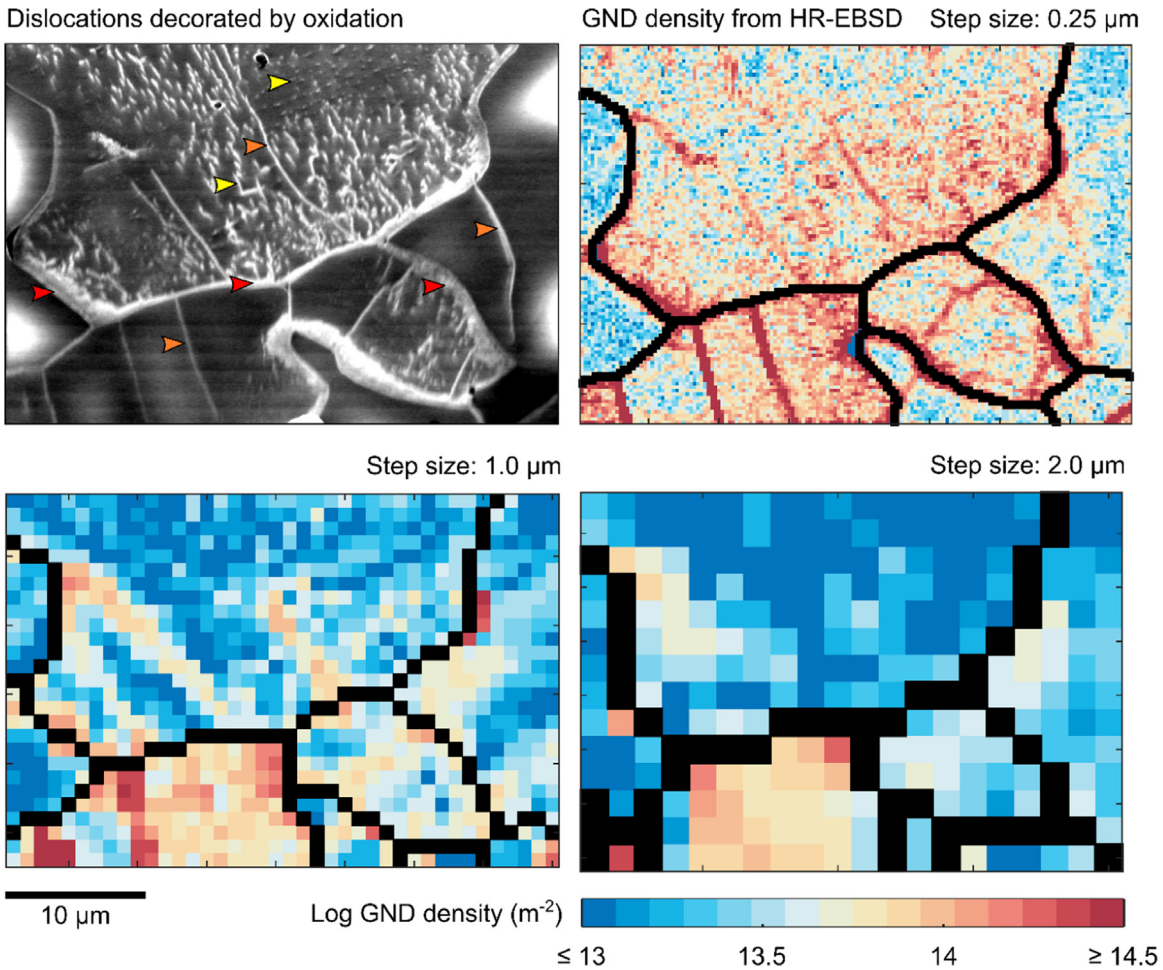

Fig. 6. Dislocations (e.g. yellow arrows), subgrain boundaries (e.g. orange arrows) and grain boundaries (e.g. red arrows) imaged using oxidation decoration (forescattered electron signal) and HR-EBSD methods in specimen PT-0652. The highest spatial resolution EBSD map contains 157×108 points at 0.25 μm step size and 2×2 EBSP pixel binning. This dataset was under-sampled and results re-calculated to generate maps with 1.0 μm and 2.0 μm step sizes. (For interpretation of the references to color in this figure legend, the reader is referred to the web version of this article.)

size is $< 3 \times 10^{13}$ m^{-2} (Fig. 5), and therefore most of the map in Fig. 6 corresponds to meaningful signal.

Fig. 6 also depicts the change in spatial resolution as step size is varied. As step size is increased to 1.0 μm, finely distributed dislocations are no longer spatially resolved, but structures characterised by higher GND densities can still be identified. At 2.0 μm step size, only the most prominent boundaries are spatially resolved. In general, the GND densities in the maps progressively decrease with increasing step size, consistent with the trends presented in Fig. 5.

4. Discussion

4.1. Advantages of applying HR-EBSD to olivine

HR-EBSD offers significant advantages over conventional EBSD for detailed analysis of olivine deformation, in particular for analysis of dislocation structures that yield low misorientation angles. The EBSP cross-correlation approach provides dramatically improved angular resolution compared to Hough transform-based analysis [9,13,14,47]. The reduced noise floor allows low-angle boundaries to be more clearly resolved, as demonstrated in Fig. 1, and provides sensitivity to GND densities on the order of 10^{11} m^{-2} at large step sizes of ~10–20 μm (Fig. 5). The minimum GND densities confidently observable by the Hough transform-based analysis will be 2–3 orders of magnitude larger. Furthermore, the GND content can be divided into different dislocation types based on their resulting curvatures (Fig. 7) [9]. This subdivision is possible because HR-EBSD allows both misorientation angles and axes orientations to be determined simultaneously and precisely, even for small misorientations of 1° or less [58], which is not possible by conventional EBSD analysis [59]. The only other method that can distinguish dislocation types is TEM, however, HR-EBSD offers the advantages of analysing larger length-scales, often including multiple grains with ease, and requiring simpler specimen preparation.

The ability to distinguish dislocation types allows analysis of the roles of different dislocation types in forming intragranular substructure and, more generally, of different slip systems in accommodating crystal plastic deformation. For example, Fig. 7 presents GND densities for individual dislocation types in a deformed single crystal of olivine (sample PI-1433). Dislocations with [100] Burgers vectors generally have the greatest densities, consistent with this being the most easily activated slip direction in olivine [40,41,53]. Two approximately perpendicular sets of structures are also apparent, one predominantly in the maps of (001)[100] edge and [100] screw dislocations, and the other in the (010)[001] maps. These structures can each be interpreted as slip bands in orientations appropriate for the respective dislocation types (Fig. 7). This crystal was intentionally oriented to predominantly activate (010)[001] dislocations during the deformation experiment, and so it might be unintuitive that high densities of (001)[100] dislocations are present. However, although the (001)[100] slip system has a relatively low Schmid factor (0.24), the large applied stress (388 MPa) results in significant resolved shear stress on this slip system (93 MPa). Other boundaries are present in maps for multiple dislocation types, indicating they are more general in nature (Fig. 7).

HR-EBSD also has advantages for characterising dislocation content over the traditional method of direct observation by oxidation decoration. Not only can the dislocation types be more readily determined as discussed above, but there are also more subtle benefits regarding the observable dislocation densities. Superficially, it might be expected that decoration would reveal the full dislocation content, i.e. both GNDs and SSDs, whereas the HR-EBSD approach used here only detects GNDs and therefore should yield lower densities than observed by decoration. However, our comparison of these two methods (Fig. 6) demonstrates that there is significant dislocation content revealed in the HR-EBSD-derived GND density map that is not evident in the image of decorated dislocations. There are both dislocations distributed throughout the grains and dislocations arranged into subgrain boundaries that are only observed in the GND density maps

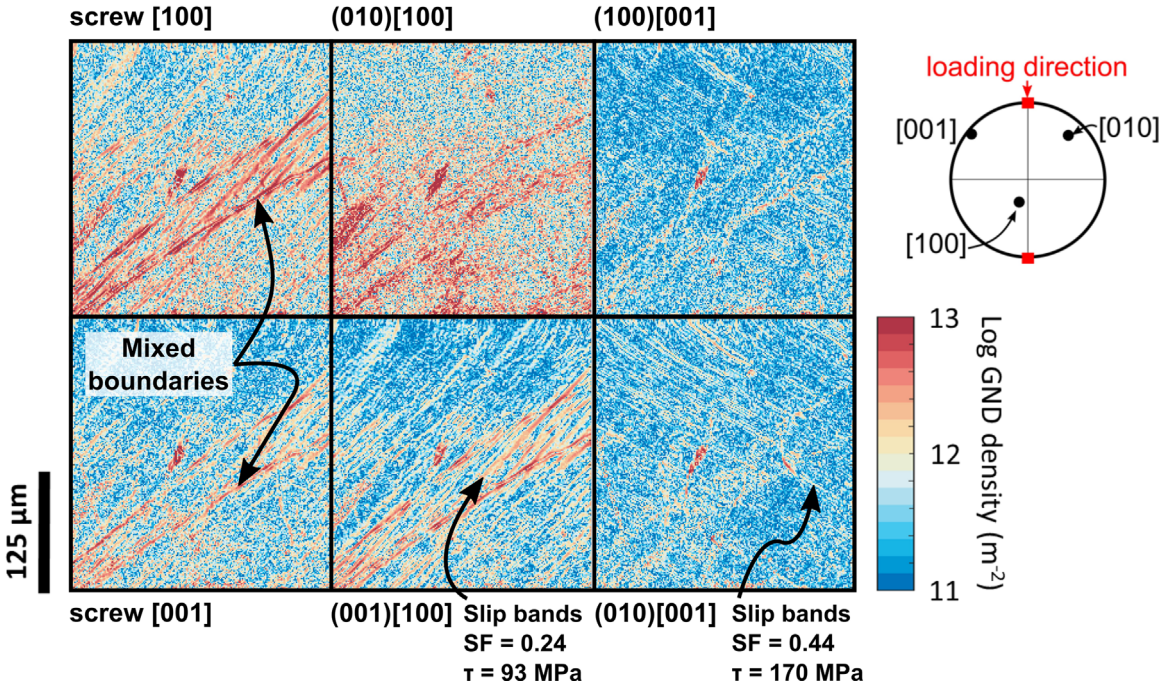

Fig. 7. GND densities of individual dislocation types in olivine sample PI-1433. The character of the most prominent structures, interpreted from dislocation type, crystal orientation and loading direction are shown, along with the Schmid factor (SF) and resolved shear stress (τ) on the relevant slip systems. (For interpretation of the references to color in this figure, the reader is referred to the web version of this article.)

(Fig. 6). We attribute this difference to the necessity for connectivity of diffusive pathways to the surface during oxidation. That is, some dislocations lacked a rapid diffusion pathway to the specimen surface during oxidation and failed to decorate sufficiently. Thus, HR-EBSD provides a method for analysing dislocation content that is less dependent on specimen geometry/preparation effects than traditional oxidation decoration and may reveal structure that would otherwise be undetected.

It is pertinent to note that the HR-EBSD method for deriving GND densities is better determined when applied to orthorhombic olivine than it is for typical applications in higher symmetry materials, such as cubic or hexagonal metals, and therefore specific dislocation types can be resolved [48,49]. Such an advantage had been noted by Reddy et al. [15] in Hough-based EBSD analysis of zircon. This improvement results from the relatively small number of available slip systems in olivine. Because of the long [010] direction precluding slip with that Burgers vector, and the lower crystal symmetry, olivine only readily exhibits six dislocation types (accounting for screw and edge dislocations), whereas materials previously explored with HR-EBSD tend to have ≥ 16 dislocation types. With only six dislocation types, $\mathbf{A}$ is a 6×6 matrix, and the inverse problem is therefore fully constrained with a unique solution. Because least-squares inversion (pinv6) yields the most reliable results in our sensitivity tests (Figs. 2 and 3), GND estimation in olivine can avoid the energy minimising approach that has been implemented in the poorer constrained metallic systems (e.g. bcc iron [9], fcc copper [48], fcc nickel [60], hcp titanium [49]).

The results of our orientation testing demonstrate that GND density estimation is accurate for a wide range of specimen surface orientations in crystal space. The principle exceptions are edge dislocations with Burgers vectors normal to the specimen surface, which result in no measurable curvature, and screw dislocations with Burgers vectors in or near the specimen plane, for which the full curvature is not detectable (Figs. 2 and 4), in accord with [8]. This orientation dependence is important to note during experimental design as single crystals, or polycrystals with strong crystal preferred orientation, can be sectioned such that the specimen surface is in a favourable orientation, thereby ensuring accurate estimation of the GND density.

4.2. Optimising EBSD data acquisition for GND analysis

Jiang et al. [47] investigated the variation in apparent GND densities in undeformed silicon and deformed copper as a function of step size in the range 0.5–10 μm. They found that, in this range, the apparent GND density decreased with step size. They attributed this effect to increasing proportions of the dislocation population appearing as SSDs as the step size increased. That is, at larger step sizes, there is a higher likelihood that pairs of dislocations exist between the measurement points with curvatures summing to zero (e.g., a dislocation dipole). This effect is also borne out by our olivine and silicon data up to step sizes of $\sim$20 μm (Fig. 5).

Clearly, to resolve low GND densities, large step sizes are beneficial. However, increased step size results in a concomitant loss of spatial resolution of dislocation structures (Fig. 6). Therefore, small step sizes are required to resolve short length-scale and high GND density substructures, such as subgrain boundaries. We note that the subsampling approach adopted in this study allows both end members to be investigated and the optimal balance to be determined, while requiring the acquisition of only one dataset. Furthermore, since EBSP binning has a relatively minimal effect on estimated GND density in deformed samples with significant dislocation content (Fig. 5) [47], increased binning offers an effective means to increase mapping speed and facilitate collection of high spatial resolution datasets in manageable mapping times.

4.3. Future applications

HR-EBSD provides the capability to quantitatively analyse olivine GND densities and their distributions for all dislocation types and over a wide range of length scales. Although the density of decorated dislocations has been demonstrated to be proportional to differential stress during deformation [40,41], HR-EBSD offers potential to derive and apply new piezometric relationships based on GND density that may be applied more reproducibly and quantitatively to olivine. This approach may potentially also be applied to other minerals whose dislocations are not easily decorated. GND distributions derived from HR-EBSD maps may be used similarly to infer differential stress based on existing subgrain-size piezometers [40,43]. More generally, GND distributions may be used to develop and/or test models for the role of dislocations during creep. Moreover, the ability to distinguish the densities and distributions of individual types of dislocation offers opportunities to investigate changes in slip system activity and dislocation behaviour under variable environmental and mechanical conditions.

5. Conclusions

We have applied the HR-EBSD technique to olivine, the dominant mineral in Earth's upper mantle, to determine GND densities and distributions associated with creep. This technique has much greater angular resolution ($<0.01°$) than conventional EBSD ($\sim$0.5°), allowing lower angle substructures to be resolved [13]. Tests of a range of methods for estimating GND density from orientation gradients demonstrate that GND densities in olivine can be recovered without the need for additional constraining assumptions typically employed for analysis of higher symmetry metals. Comparison of HR-EBSD-derived GND density maps to electron images of samples with dislocations decorated by oxidation demonstrates that HR-EBSD can successfully characterise areas in which dislocations are distributed and areas in which they are localised into subgrain boundaries. Moreover, HR-EBSD reveals information not captured by the decoration technique, such as the presence of dislocation structures that failed to decorate during oxidation.

As apparent GND density decreases with increasing step size, data acquisition can be optimised for resolving either long wavelength, low amplitude orientation gradients or shorter length scale, high GND density structures such as subgrain boundaries.

HR-EBSD offers a new approach to investigate microstructural characteristics with geodynamic significance. The ability to estimate dislocation densities and length scales of subgrain structures gives potential to apply and develop palaeopiezometric techniques, and the ability to distinguish dislocation types offers new opportunities to investigate variations in slip system activity and the role of dislocations in a range of creep regimes.

Acknowledgements

David Kohlstedt generously contributed deformed single crystals for characterisation. The authors are grateful to John Wheeler for the use of his software to calculate components of the dislocation density tensor from conventional EBSD data. We thank Nick Timms for his constructive review of the manuscript. D. Wallis, L. Hansen and A.J. Wilkinson acknowledge support from the Natural Environment Research Council Grant NE/M000966/1. T.B. Britton acknowledges support for his research fellowship from the Royal Academy of

Engineering. Research data supporting this paper can be found on the Oxford Research Archive (http://www.ora.ox.ac.uk/).

References

[1] P.B. Hirsch, A. Howie, M.J. Whelan, A kinematic theory of diffraction contrast of electron transmission microscope images of dislocations and other defects, Philos. Trans. R. Soc. Lond. Ser. A – Math. Phys. Sci. 252 (1960) 499–529.
[2] D.L. Kohlstedt, C. Goetze, W.B. Durham, J. Vandersande, New technique for decorating dislocations in olivine, Science 191 (1976) 1045–1046.
[3] S. Karato, Scanning electron microscope observation of dislocations in olivine, Phys. Chem. Miner. 14 (1987) 245–248.
[4] R.J.M. Farla, H. Kokkonen, J.D.F. Gerald, A. Barnhoorn, U.H. Faul, I. Jackson, Dislocation recovery in fine-grained polycrystalline olivine, Phys. Chem. Miner. 38 (2011) 363–377.
[5] S. Sun, B.L. Adams, W.E. King, Observations of lattice curvature near the interface of a deformed aluminium bicrystal, Philos. Mag. 80 (2000) 9–25.
[6] B.S. El-Dasher, B.L. Adams, A.D. Rollett, Viewpoint: experimental recovery of geometrically necessary dislocation density in polycrystals, Scr. Mater. 48 (2003) 141–145.
[7] W. Pantleon, Resolving the geometrically necessary dislocation content by conventional electron backscattering diffraction, Scr. Mater. 58 (2008) 994–997.
[8] J. Wheeler, E. Mariani, S. Piazolo, D.L. Prior, P. Trimby, M.R. Drury, The weighted Burgers vector: a new quantity for constraining dislocation densities and types using electron backscatter diffraction on 2D sections through crystalline materials, J. Microsc. 233 (2009) 482–494.
[9] A.J. Wilkinson, D. Randman, Determination of elastic strain fields and geometrically necessary dislocation distributions near nanoindents using electron back scatter diffraction, Philos. Mag. 90 (2010) 1159–1177.
[10] T.B. Britton, S. Birosca, M. Preuss, A.J. Wilkinson, Electron backscatter diffraction study of dislocation content of a macrozone in hot-rolled Ti–6Al–4V alloy, Scr. Mater. 62 (2010) 639–642.
[11] J. Jiang, T.B. Britton, A.J. Wilkinson, Evolution of dislocation density distributions in copper during tensile deformation, Acta Mater. 61 (2013) 7227–7239.
[12] C.F.O. Dahlberg, Y. Saito, M.S. Öztop, J.W. Kysar, Geometrically necessary dislocations density measurements associated with different angles on indentations, Int. J. Plast. 54 (2014) 81–95.
[13] A.J. Wilkinson, G. Meaden, D. Dingley, High resolution mapping of strains and rotations using electron backscatter diffraction, Mater. Sci. Technol. 22 (2006) 1271–1278.
[14] S. Villert, C. Maurice, C. Wyon, R. Fortunier, Accuracy assessment of elastic strain measurement by EBSD, J. Microsc. 233 (2009) 290–301.
[15] S.M. Reddy, N.E. Timms, W. Pantleon, P. Trimby, Quantitative characterisation of plastic deformation of zircon and geological implications, Contrib. Mineral. Petrol. 153 (2007) 625–645.
[16] M.A. Billia, N.E. Timms, V.G. Toy, R.D. Hart, D.J. Prior, Grain boundary dissolution porosity in quartzofeldspathic ultramylonites: implications for permeability enhancement and weakening of mid-crustal shear zones, J. Struct. Geol. 53 (2013) 2–14.
[17] S. Karato, P. Wu, Rheology of the upper mantle: a synthesis, Science 260 (1993) 771–778.
[18] P.J. Tackley, Mantle convection and plate tectonics: toward an integrated physical and chemical theory, Science 288 (2000) 2002–2007.
[19] A. Rozel, Impact of grain size on the convection of terrestrial planets, Geochem. Geophys. Geosyst. 13 (2012) Q10020.
[20] K. Michibayashi, D. Mainprice, The role of pre-existing mechanical anisotropy on shear zone development within oceanic mantle lithosphere: an example from the oman ophiolite, J. Petrol. 45 (2004) 405–414.
[21] J.M. Warren, G. Hirth, Grain size sensitive deformation mechanisms in naturally deformed peridotites, Earth Planet. Sci. Lett. 248 (2006) 438–450.
[22] M.I. Billen, G. Hirth, Rheologic controls on slab dynamics, Geochem. Geophys. Geosyst. 8 (2007) Q08012.
[23] W.B. Durham, C. Goetze, Plastic flow of oriented single crystal of olivine 1. Mechanical data, J. Geophys. Res. 82 (1977) 5737–5753.
[24] P.N. Chopra, M.S. Paterson, The role of water in the deformation of dunite, J. Geophys. Res. 89 (1984) 7861–7876.
[25] G. Hirth, D.L. Kohlstedt, Experimental constraints on the dynamics of the partially molten upper mantle 2. Deformation in the dislocation creep regime, J. Geophys. Res.: Solid Earth 100 (1995) 15441–15449.
[26] J.W. Keefner, S.J. Mackwell, D.L. Kohlstedt, F. Heidelbach, Dependence of dislocation creep of dunite on oxygen fugacity: implications for viscosity variations in Earth's mantle, J. Geophys. Res. 116 (2011) B05201.
[27] G. Hirth, D.L. Kohlstedt, Experimental constraints on the dynamics of the partially molten upper mantle 2. Deformation in the diffusion creep regime, J. Geophys. Res.: Solid Earth 100 (1995) 1981–2001.
[28] S. Mei, D.L. Kohlstedt, Influence of water on plastic deformation of olivine aggregates 1. Diffusion creep regime, J. Geophys. Res.: Solid Earth 105 (2000) 21457–21469.
[29] G. Hirth, D.L. Kohlstedt, Rheology of the mantle wedge: a view from the experimentalists, in: J. Eiler (Ed.), Inside the Subduction Factory, Geophysical Monograph Series, AGU, Washington D.C., 2003, pp. 83–105.
[30] L.N. Hansen, M.E. Zimmerman, D.L. Kohlstedt, Grain boundary sliding in San Carlos olivine: flow law parameters and crystallographic-preferred orientation, J. Geophys. Res.: Solid Earth 116 (2011) B08201.
[31] T. Miyazaki, K. Sueyoshi, T. Hiraga, Olivine crystals align during diffusion creep of Earth's upper mantle, Nature 502 (2013) 321–326.
[32] T. Ohuchi, T. Kawazoe, Y. Higo, K. Funakoshi, A. Suzuki, T. Kikegawa, T. Irifune, Dislocation-accommodated grain boundary sliding as the major deformation mechanism of olivine in the Earth's upper mantle, Sci. Adv. 1 (2015) e1500360.
[33] C.B. Raleigh, Glide mechanisms in experimentally deformed minerals, Science 150 (1965) 739–741.
[34] M.W. Wegner, J.J. Grossman, Dislocation etching of naturally deformed olivine, Trans. – Am. Geophys. Union 50 (1969) 676.
[35] C. Young, Dislocations in the deformation of olivine, Am. J. Sci. 267 (1969) 841–852.
[36] J.N. Boland, A.C. McLaren, B.E. Hobbs, Dislocations associated with optical features in naturally-deformed olivine, Contrib. Mineral. Petrol. 30 (1971) 53–63.
[37] J.D. Blacic, J.M. Christie, Dislocation substructure of experimentally deformed olivine, Contrib. Mineral. Petrol. 42 (1973) 141–146.
[38] C. Goetze, D.L. Kohlstedt, Laboratory study of dislocation climb and diffusion in olivine, J. Geophys. Res. 78 (1973) 5961–5971.
[39] J.B. Vander Sande, D.L. Kohlstedt, Observation of dissociated dislocations in deformed olivine, Philos. Mag. 34 (1976) 653–658.
[40] W.B. Durham, C. Goetze, B. Blake, Plastic flow of oriented single crystals of olivine 2. Observations and interpretations of the dislocation structures, J. Geophys. Res. 82 (1977) 5755–5770.
[41] Q. Bai, D.L. Kohlstedt, High-temperature creep of olivine single crystals, 2. Dislocation structures, Tectonophysics 206 (1992) 1–29.
[42] D.H. Zeuch, H.W. Green, Naturally decorated dislocations in olivine from peridotite xenoliths, Contrib. Mineral. Petrol. 62 (1977) 141–151.
[43] M. Toriumi, Relation between dislocation density and subgrain size of naturally deformed olivine in peridotites, Contrib. Mineral. Petrol. 68 (1979) 181–186.
[44] A. Mussi, P. Cordier, S. Demouchy, Characterisation of dislocation interactions in olivine using electron tomography, Philos. Mag. 95 (2015) 335–345.
[45] C.L. Johnson, M.J. Hÿtch, P.R. Buesck, Displacement and strain fields around a [100] dislocation in olivine measured to sub-angstrom accuracy, Am. Mineral. 89 (2004) 1374–1379.
[46] T.B. Britton, A.J. Wilkinson, Measurement of residual elastic strain and lattice rotations with high resolution electron backscatter diffraction, Ultramicroscopy 2011 (2011) 1395–1404.
[47] J. Jiang, T.B. Britton, A.J. Wilkinson, Measurement of geometrically necessary dislocation density with high resolution electron backscatter diffraction: effects of detector binning and step size, Ultramicroscopy 125 (2013) 1–9.
[48] J. Jiang, T.B. Britton, A.J. Wilkinson, Accumulation of geometrically necessary dislocations near grain boundaries in deformed copper, Philos. Mag. Lett. 92 (2012) 580–588.
[49] T.B. Britton, A.J. Wilkinson, Stress fields and geometrically necessary dislocation density distributions near the head of a blocked slip band, Acta Mater. 60 (2012) 5773–5782.
[50] P.D. Littlewood, T.B. Britton, A.J. Wilkinson, Geometrically necessary dislocation density distributions in Ti–6Al–4V deformed in tension, Acta Mater. 59 (2011) 6489–6500.
[51] J. Villanova, C. Maurice, J.-S. Micha, P. Bleuet, O. Sicardy, R. Fortunier, Multiscale measurements of residual strains in a stabilized zirconia layer, J. Appl. Crystallogr. 45 (2012) 926–935.
[52] E.H. Abramson, J.M. Brown, L.J. Slutsky, J. Zaug, The elastic constants of San Carlos olivine to 17 GPa, J. Geophys. Res. 102 (1997) 12,253–12,263.
[53] A. Tommasi, D. Mainprice, G. Canova, Y. Chastel, Viscoplastic self-consistent and equilibrium-based modeling of olivine lattice preferred orientations: implications for the upper mantle seismic anisotropy, J. Geophys. Res.: Solid Earth 105 (2000) 7893–7908.
[54] E. Kroner, Continuum theory of dislocations and self-stresses, Ergeb. Angew. Math. 5 (1958) 1327–1347.
[55] J.F. Nye, Some geometrical relations in dislocated crystals, Acta Metall. 1 (1953) 153–162.
[56] L.N. Hansen, M.E. Zimmerman, D.L. Kohlstedt, Laboratory measurements of the viscous anisotropy of olivine aggregates, Nature 492 (2012) 415–418.
[57] D.P. Field, P.B. Trivedi, S.I. Wright, M. Kumar, Analysis of local orientation gradients in deformed single crystal, Ultramicroscopy 103 (2005) 33–39.
[58] A.J. Wilkinson, A new method for determining small misorientations from electron back scatter diffraction patterns, Scr. Mater. 44 (2001) 2379–2385.
[59] D.J. Prior, Problems in determining the misorientation axes, for small angular misorientations, using electron backscatter diffraction in the SEM, J. Microsc. 195 (1999) 217–225.
[60] P.S. Karamched, A.J. Wilkinson, High resolution electron back-scatter diffraction analysis of thermally and mechanically induced strains near carbide inclusions in a superalloy, Acta Mater. 59 (2011) 263–272.